

Work Plan - AJIF Project: Conversion of CO₂ into Methanol via an Innovative Photocatalytic and Electrocatalytic Process for Sustainable Energy Applications

Marco Fronzi¹, Paolo Mele²,
Fabio Lisi³, Shivani Sathgish⁴, Catherine Stampfl¹

¹University of Sydney, Australia

²Shibaura Institute of Technology, Japan

³University of Tokyo, Japan

⁴Atierra, Japan

1 Introduction

The rapid increase in atmospheric carbon dioxide (CO₂) concentration represents one of the most urgent environmental challenges of our time. Since the industrial revolution, global CO₂ levels have risen dramatically, driving climate change and its associated risks such as extreme weather events and ecosystem disruption. Strategies to mitigate this trend increasingly emphasise not only CO₂ capture but also its conversion into value-added products. Among various utilisation pathways, hydrogenation of CO₂ to methanol has emerged as a particularly promising option due to methanol's role as a platform molecule in fuels, energy storage, and the chemical industry.

Methanol offers several advantages: it can serve directly as a clean fuel, as a hydrogen carrier, and as a precursor for the synthesis of olefins, aromatics, and other chemicals. Its integration into the energy system aligns with the concept of a “methanol economy,” which envisions recycling CO₂ into fuels and chemicals, thereby reducing reliance on fossil resources. Despite these prospects, the large-scale deployment of CO₂-to-methanol technology remains constrained by challenges such as high reaction pressures, catalyst deactivation, and the need for inexpensive, sustainable hydrogen sources.

Considerable progress has been made in understanding and improving catalytic performance. Cu/ZnO-based catalysts remain the benchmark for industrial methanol synthesis, where the synergy between Cu and ZnO interfaces is recognised as critical for CO₂ activation and intermediate stabilisation. Beyond conventional systems, novel catalyst designs—such as In₂O₃-based oxides, bimetallic interfaces, and hybrid carbon-supported nanostructures—have demonstrated promising activity and selectivity. In particular, two-dimensional (2D) materials like graphene and reduced graphene oxide (rGO) offer unique opportunities to engineer active interfaces with transition metal oxides, enhancing charge transfer and stabilising defect structures.

This report builds upon these advances by investigating CuO- and AgO-based catalysts supported on graphene platforms. Through a combined computational-experimental approach, the study aims to correlate band structure descriptors, such as *d*-band centre positions, with catalytic performance. By systematically analysing hybrid 2D/oxide heterostructures, we seek to contribute new insights into the rational design of catalysts for efficient and sustainable CO₂ hydrogenation to methanol.

2 Theoretical-computational analysis

2.1 Overview

The theoretical component of this project focuses on understanding the atomistic and electronic behaviour of CuO and AgO monolayers on graphene using density functional theory (DFT). These calculations provide insights into interfacial bonding, band alignment, charge redistribution, and light absorption properties. By modelling both ideal bilayer heterostructures and realistic clusters, we aim to determine which configurations are structurally stable and electronically suitable for CO₂ activation. Results from this section also guide the design of experimental structures by highlighting the key factors that govern interfacial reactivity and electronic coupling.

2.2 Computational Methodology

Density functional theory (DFT) calculations were performed with VASP [1, 2] using the projector augmented wave (PAW) method [3, 4] and the PBE exchange-correlation functional [5]. A plane-wave cutoff of 550 eV ensured energy convergence within 1 meV/atom. Electronic self-consistency was achieved to 10⁻⁶ eV, and atomic positions were relaxed by the conjugate-gradient algorithm until forces were below 0.01 eV/Å.

Van der Waals interactions, essential for graphene-based systems, were treated with Grimmes D3 correction and Becke-Johnson damping [6]. Brillouin-zone sampling employed Γ -centered k -meshes with typical spacing $\leq 0.03 \text{ \AA}^{-1}$. For large supercells (> 100 atoms), Γ -point-only sampling was used during relaxations.

Projected DOS (pDOS) were obtained with denser k -grids: $3 \times 3 \times 1$ for bilayers and $2 \times 2 \times 1$ for cluster-decorated graphene, depending on cell size. Wavefunctions were projected onto spherical harmonics within PAW spheres to yield *s*-, *p*-, and *d*-orbital contributions. Gaussian smearing (0.05 eV) was applied for visualization.

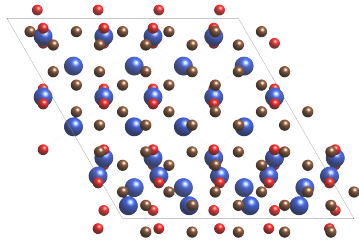
The *d*-band center, ε_d , was calculated as the first moment of the *d*-projected DOS relative to the Fermi level:

$$\varepsilon_d = \frac{\int E n_d(E) dE}{\int n_d(E) dE}, \quad (1)$$

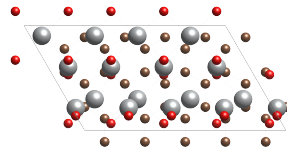
with $n_d(E)$ the *d*-orbital DOS and E referenced to E_F , providing a descriptor of adsorbate binding strength within the *d*-band model [7].

2.3 Model Systems

The core of this work focuses on bilayer heterostructures composed of **graphene with CuO** and **graphene with AgO**. These combinations were chosen due to their established redox reactivity, polar surfaces, and chemical stability under ambient conditions. By constraining the lattice mismatch to below 7%, the constructed bilayer supercells provide physically realistic strain environments for subsequent electronic and catalytic analysis. Figure 1 shows representative relaxed geometries after optimisation.



(a) Graphene/CuO bilayer.



(b) Graphene/AgO bilayer.

Figure 1: Optimised geometries of graphene/metal oxide bilayers (DFT-GGA-PBE, 20 Å vacuum).

2.4 Supporting Model Systems

In realistic synthesis environments (e.g. sputtering, solution deposition), oxide deposition on graphene can yield not only uniform 2D layers but also nanoclusters and islands. To reflect this, we included additional structural motifs:

- Graphene-oxide bilayers with varying orientations and mismatches.
- Graphene decorated with CuO and AgO nanoparticles to mimic experimental film growth.
- Graphene interfaced with metallic clusters (Cu_n , Ag_n), capturing possible reduction products of the oxides.

This broader set of models allows us to distinguish between idealised flat bilayers and cluster-induced reconstructions, providing a more complete framework for interpreting experimental characterisation. Figure 2 illustrates typical relaxed cluster-graphene structures.

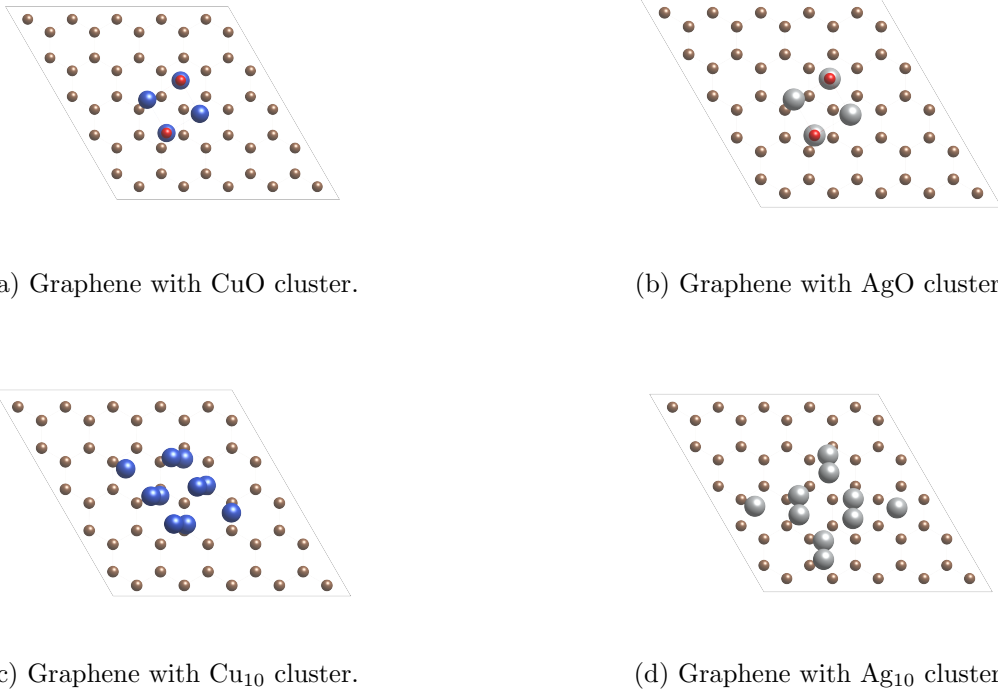


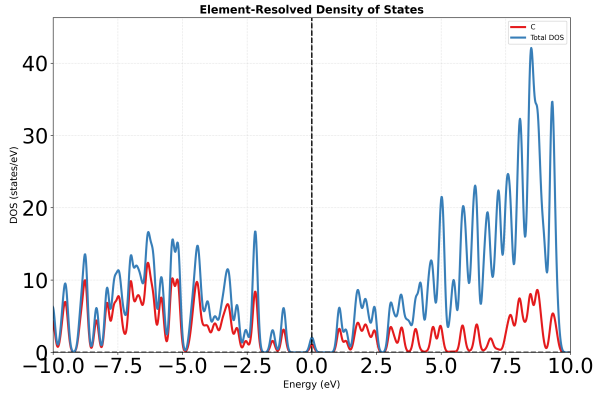
Figure 2: Representative cluster-decorated graphene structures after DFT relaxation.

3 Electronic and Optical Analysis

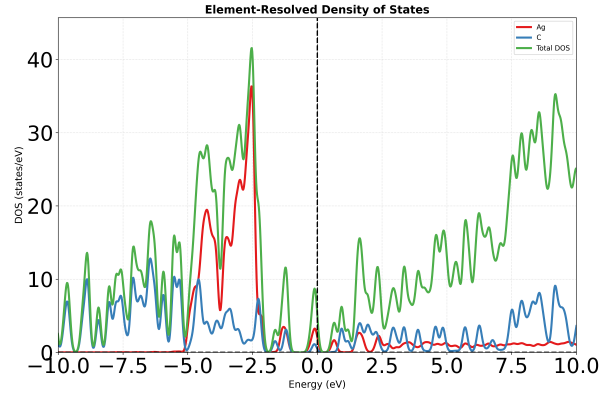
The electronic structures of graphene and hybrid systems were examined via projected density of states (pDOS). Pristine graphene exhibits the characteristic linear dispersion around the Dirac point, which ideally results in a vanishing DOS at the Fermi level. In practice, however, the calculated pDOS shows a small but finite DOS at E_F , arising from numerical smearing, finite k -point sampling, and supercell effects. This feature does not alter the overall semimetallic character of graphene, but it is important to recognise when interpreting computational results against experimental data.

Decorating graphene with Ag_{10} clusters introduces Ag-states in the 5 to -2.5 eV range, with additional localized peaks around -1 eV and right below Fermi Energy. These hybridise only weakly with graphene p_z orbitals and contribute little at E_F , consistent with Ag's low catalytic activity in CO_2 reduction. Cu clusters (Cu_7 , Cu_{10}) shift the broad Cu-bands closer to E_F (-2 to -1 eV). This indicates enhanced charge transfer capability and stronger chemisorption potential, with the effect more pronounced for Cu_{10} .

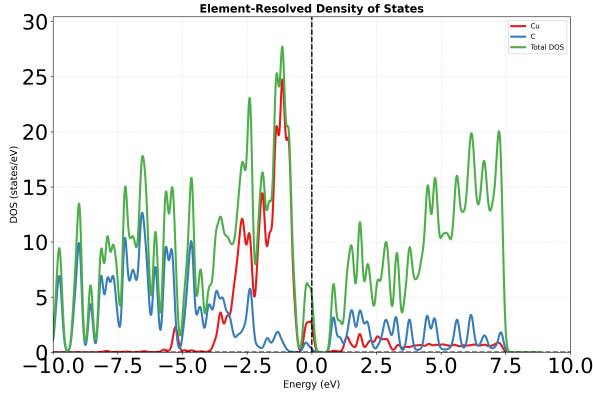
Oxide-decorated systems further enrich the electronic landscape. CuO clusters introduce new states from -6 to -4 eV that overlap with Cu-states, broadening the valence band and generating mid-gap states relevant for CO_2 activation. AgO bilayers add broad O/Ag bands with moderate DOS at E_F , suggesting improved reactivity compared to metallic Ag but still weaker than Cu-based systems. These results highlight that Cu-based hybrids, particularly larger clusters and CuO composites, shift the electronic structure to favour adsorption and activation processes, while Ag-based systems contribute less effectively to states near the Fermi level.



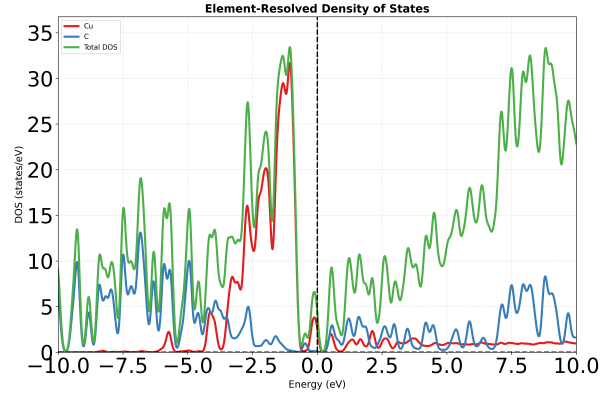
(a) Pristine graphene.



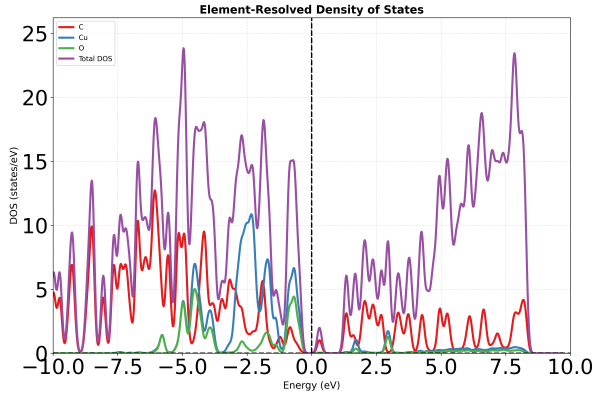
(b) Ag_{10} cluster on graphene.



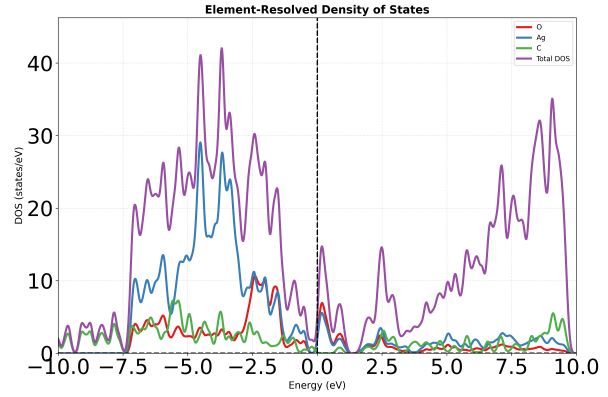
(c) Cu_7 cluster on graphene.



(d) Cu_{10} cluster on graphene.



(e) CuO cluster on graphene.



(f) Graphene-AgO bilayer.

Figure 3: Orbital-resolved pDOS for graphene and hybrid systems. Cu clusters shift d -bands closer to E_F and yield finite DOS at the Fermi level, enhancing reactivity. CuO and AgO introduce oxygen-derived states that broaden the valence band. Ag-based systems display broader but weaker d -contributions.

4 Electronic Band Centres and Implications for $\text{CO}_2 \rightarrow \text{CH}_3\text{OH}$ Catalysis

Table 1 reports the centres of the *s*-, *p*-, and *d*-projected bands (in eV, relative to E_F) for graphene-based bilayers and selected metal/oxide hybrids. In what follows we focus on the *d*-band centre, a widely used descriptor for adsorption and catalytic activity on transition-metal sites.¹

Table 1: Centres of the *s*-, *p*-, and *d*-projected bands (eV vs. E_F).

Bilayer / Material	<i>s</i> -band	<i>p</i> -band	<i>d</i> -band
Graphene	−3.737	−2.413	0.000
Graphene-Ag ₁₀	−0.488	−1.783	−3.166
Graphene-Cu ₁₀	−0.825	−1.817	−1.678
Graphene-Cu ₇	−1.207	−1.997	−1.559
Graphene-CuO (cluster)	−1.493	−2.258	−2.285
Graphene-AgO (bilayer)	−0.650	−2.052	−3.698

What the *d*-band centre means

Within the Newns-Anderson/Hammer-Nrskov picture, the energy of the metal *d*-states relative to E_F governs the strength of adsorbate-metal coupling: a *higher* (less negative) *d*-band centre generally correlates with *stronger* adsorption because the antibonding states formed upon chemisorption are less occupied.[8, 9] Practically, moving the *d*-band centre upward (towards E_F) tends to strengthen binding of key intermediates (e.g. *CO₂, *HCOO, *CO, *H, *O), while shifting it downward weakens their binding. The catalytic sweet spot follows Sabatiers principle: intermediates must bind neither too strongly (poisoning/slow desorption) nor too weakly (difficult activation).

Trends observed here

From Table 1:

- **Cu/graphene** (Graphene-Cu₁₀, Graphene-Cu₇) exhibits relatively *shallow* *d*-band centres (−1.68 to −1.56 eV), i.e. closer to E_F than CuO or Ag-based systems. This suggests stronger adsorption on Cu sites supported by graphene.
- **CuO/graphene** is deeper (−2.29 eV) than Cu/graphene, consistent with more oxide-like character and somewhat weaker *metallic* *d*-state participation in binding.
- **Ag-containing systems** (Graphene-Ag₁₀ at −3.17 eV; rGO-AgO at −3.70 eV) show *deep* *d*-bands, indicating generally *weak* binding on Ag sites; any CO₂ activation is more likely to originate from oxide sites (e.g. AgO) or vacancy-rich supports rather than Ag *d*-states.

Implications for $\text{CO}_2 \rightarrow \text{CH}_3\text{OH}$

For thermocatalytic hydrogenation on Cu-based catalysts, the consensus (from Cu/ZnO and Cu/ZnO/ZrO₂ literature) is that **moderate** binding of formate/methoxy and balanced CO binding favour CH₃OH

¹Throughout, we assume the band centres are the first spectral moments of the corresponding projected density of states (pDOS) referenced to E_F .

formation; too-strong binding shifts pathways to CO or leads to site blocking, while too-weak binding limits activation.[10, 11, 12] In this light:

1. **Cu/graphene (shallower *d*):** The *d*-band centres near -1.6 eV imply relatively stronger interaction with $^*\text{CO}$ and oxygenated intermediates than oxide-rich analogues. This could *enhance* initial CO_2 activation/H-assisted steps, but risks over-stabilising $^*\text{CO}$ on extended Cu ensembles. Interface/defect engineering (e.g. limited Cu cluster size, heterointerfaces) will be important to keep CO binding in the optimal window and to promote $^*\text{HCOO}$ and $^*\text{CH}_3\text{O}$ hydrogenation sequences observed on active Cu/ZnO interfaces.[12]
2. **CuO/graphene (deeper *d*):** The deeper *d*-band suggests weaker metallic binding; here, *oxide* motifs (oxygen vacancies, Cu^+/Cu^0 sites) likely dominate CO_2 activation, consistent with reports that *oxide-metal interfaces* provide the bifunctional sites for formate formation and H_2 activation.[13]
3. **Ag/AgO systems (deep *d*):** Ags deep *d*-band intrinsically weakens adsorption on *metal* sites, often favouring CO rather than CH_3OH in hydrogenation or electroreduction. Any methanol activity on rGO-AgO will likely correlate with *oxide* defect chemistry and conductive-carbon-assisted charge transfer rather than a favourable Ag *d*-band alignment.[14]

Role of interfaces and supports. Across leading CH_3OH catalysts, **interfaces** (Cu-ZnO, Cu-ZrO₂, Pd-Zn, In₂O₃-ZrO₂) are repeatedly identified as decisive for activity and selectivity, via bifunctional mechanisms and vacancy chemistry, not just a single *d*-band descriptor.[12, 13, 14] Graphitic supports (graphene, rGO) can donate/withdraw charge and tune ensemble size, shifting the metal *d*-band and *also* stabilising oxide defects-both effects can matter in practice.[14] Thus, while the *d*-band centre provides a first-order screening metric (Cu/graphene looks promising; Ag-based looks weak on metal sites), optimisation should explicitly design *oxide-metal-carbon* junctions that realise the interfacial pathways known to favour methanol.

The *d*-band model is most predictive on clean, extended metals. In oxide-rich or strongly covalent environments (e.g. Cu^+ /vacancy sites, AgO, or nano-interfaces), local electronic structure and specific active motifs can override simple *d*-band trends. Our interpretation therefore combines *d*-band reasoning with established interfacial mechanisms for $\text{CO}_2 \rightarrow \text{CH}_3\text{OH}$.[10, 11, 12]

5 Experimental Approach Overview

The experimental portion of the project is designed to fabricate and characterise hybrid metal oxide-graphene systems that mirror the theoretical models. Using spark plasma sintering (SPS) and pulsed laser deposition (PLD), we produce rGO-Cu₂O composite films on conductive substrates. These samples are subjected to thermal post-processing and characterised via structural, optical, and electrochemical methods. The experimental workflow aims not only to validate the computational predictions but also to assess the practical viability of these materials for photocatalytic CO_2 reduction under ambient conditions.

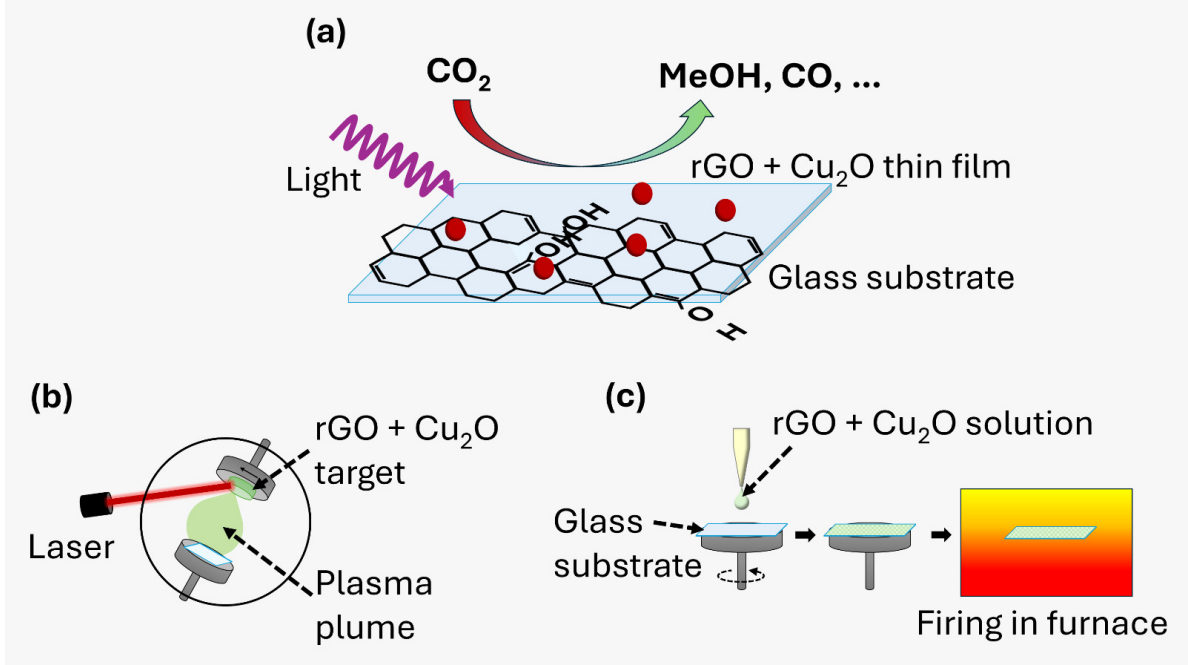


Figure 4: Schematic overview of the experimental approach for CO₂ photoreduction on rGO-Cu₂O films. (a) Conceptual diagram of CO₂ conversion under light irradiation on a rGO-Cu₂O thin film deposited on a glass substrate. (b) Pulsed Laser Deposition (PLD) setup using an rGO-Cu₂O target and laser-induced plasma plume. (c) Spin-coating process using a rGO-Cu₂O solution followed by thermal treatment in a furnace.

5.1 Experimental setup - WO₃ films

Objective: test and validate the PLD-based deposition chain by fabricating WO₃ thick films on amorphous fused silica with a thin carbon-based interlayer, and to demonstrate reproducible film growth and basic optoelectronic characterisation.

Sample preparation Two bilayer samples were prepared on amorphous fused silica substrates (size: 2 × 1 cm) by a two-step pulsed-laser deposition (PLD) process: first a carbon-based layer was deposited, then a WO₃ layer was deposited on one half of the substrate (the other half remained masked to provide an internal reference).

Carbon-layer deposition (first step)

- Laser: Nd:YAG, $\lambda = 266$ nm.
- Laser power: 800 mW.
- Reported pulse (or pulse-train) energy: 32 J (as recorded).
- Substrate temperature: 500 °C.
- Repetition rate: 10 Hz.
- Deposition time: 8 min.

- Background: high vacuum (turbo-pump base pressure $\sim 10^{-4}$ Pa).
- Cooling: natural cooling in vacuum.

WO₃ deposition (second step)

After the carbon layer deposition, half of the carbon-coated substrate was masked and the sample was reinserted in the chamber for WO₃ deposition (ablating a WO₃ target) under the following conditions:

- Laser: Nd:YAG, $\lambda = 266$ nm.
- Laser power: 440 mW.
- Reported pulse (or pulse-train) energy: 27 J (as recorded).
- Substrate temperature: 500 °C.
- Repetition rate: 10 Hz.
- Deposition times explored: 20 min and 60 min.
- Background gas: oxygen, $P_{O_2} = 27$ Pa.
- Cooling: natural cooling in oxygen.

Samples produced

1. Sample A: silica / carbon (8 min) / WO₃ (20 min).
2. Sample B: silica / carbon (8 min) / WO₃ (60 min).

6 Characterisation

6.1 Experimental Results

We performed a first validation round on carbon-coated fused-silica substrates and on bilayers including WO₃, using the PLD chain described above. The key takeaways are: (i) Raman indicates a defect-rich, graphene-like sp² carbon rather than fully amorphous carbon; (ii) UV–Vis and IR transmission are strongly suppressed by the carbon overlayer; (iii) fluorescence from the WO₃-bearing sample shows sharp features requiring re-checks; (iv) standard θ –2 θ XRD on the benchtop diffractometer only detects the substrate; and (v) next measurements should prioritise grazing-incidence XRD, XPS, and a four-point probe for film conductivity.²

²All details in this section are drawn from the project log and raw data summary shared by the team (Sept 2025).

6.2 Raman spectroscopy (primary discriminator of carbon phase)

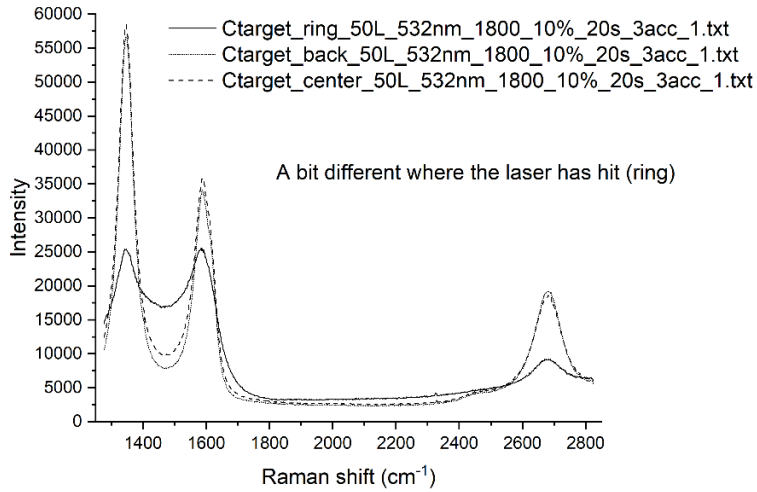


Figure 5: Raman spectrum of the carbon target collected with a short-range, high-resolution grating. Peaks at ~ 1350 , 1580 , and 2700 cm^{-1} (D, G, 2D bands) are resolved, showing defect-rich graphitic character.

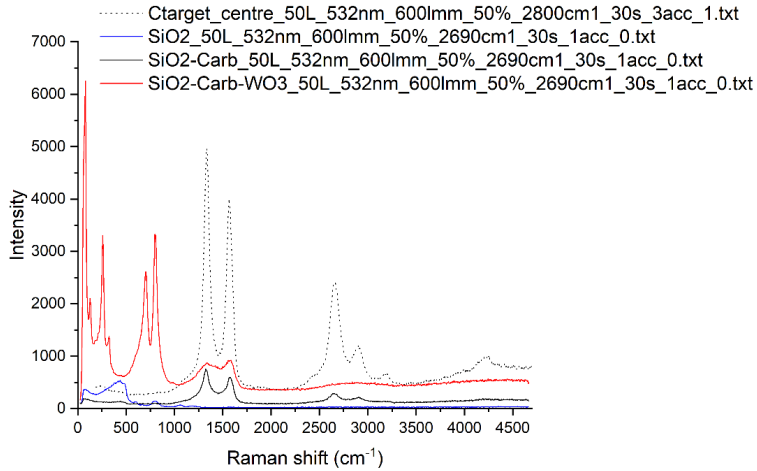


Figure 6: Wide-range Raman spectra of the carbon target, SiO₂–carbon, and SiO₂–carbon–WO₃ samples on the same intensity scale. Additional peaks appear after WO₃ deposition.

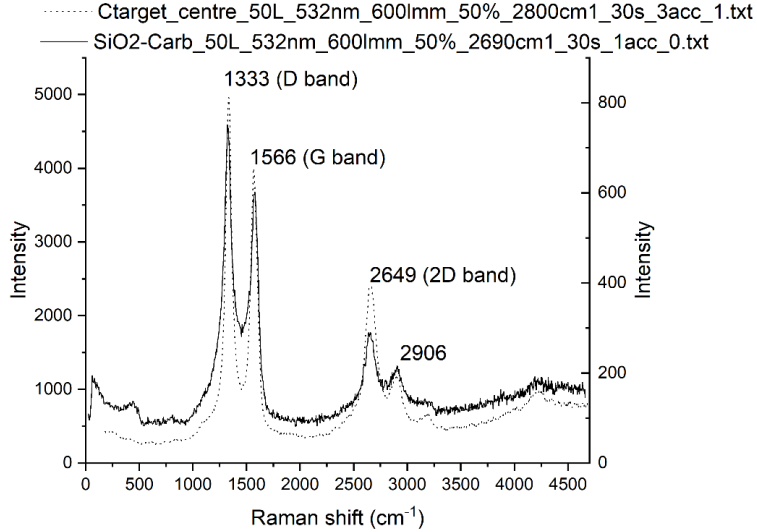


Figure 7: Overlapped Raman spectra of the carbon target and SiO_2 –carbon sample. Peak positions and intensity ratios are nearly identical, indicating transfer of carbon structure from the target to the film.

Raman spectra were collected with two gratings: a high-resolution, narrow-range one (Fig. 5), and a wide-range, lower-resolution one (Fig. 6). The D ($\sim 1350 \text{ cm}^{-1}$), G ($\sim 1580 \text{ cm}^{-1}$), and 2D ($\sim 2700 \text{ cm}^{-1}$) features are clearly resolved for both the carbon target and the SiO_2 –carbon sample (Fig. 7), with closely matching peak positions and similar intensity ratios, indicating that the deposited film reflects the target composition/structure.

Table 2: Raman intensity ratios for the carbon target and SiO_2 –carbon sample.

Specimen	I_D/I_G	I_{2D}/I_G	Interpretation
Carbon target	1.240	0.600	Defect-rich sp^2 domains (nc-graphite / rGO-like)
SiO_2 –carbon	1.259	0.486	Same class; slightly lower relative 2D intensity

The relatively large I_D/I_G (≈ 1.25) together with a visible 2D band is consistent with nanocrystalline/defective graphitic carbon (defective graphene or rGO-like), not fully amorphous a-C. Recommended next checks to tighten classification: peak positions and FWHM for G and 2D bands, D' ($\sim 1620 \text{ cm}^{-1}$) visibility, and explicit laser wavelength reporting for proper literature comparison.³

6.3 Infrared spectroscopy

ATR. The current ATR spectrum (Fig. 8) is dominated by the silica band near 900 cm^{-1} (background issue), with suspected artefacts around $\sim 2100 \text{ cm}^{-1}$. Importantly, no clear C=O stretching near $\sim 1700 \text{ cm}^{-1}$ was observed, suggesting the carbon layer is not strongly oxidised. A better background and contact optimisation are planned.

³These interpretations reflect the teams September notes and quick literature screening.

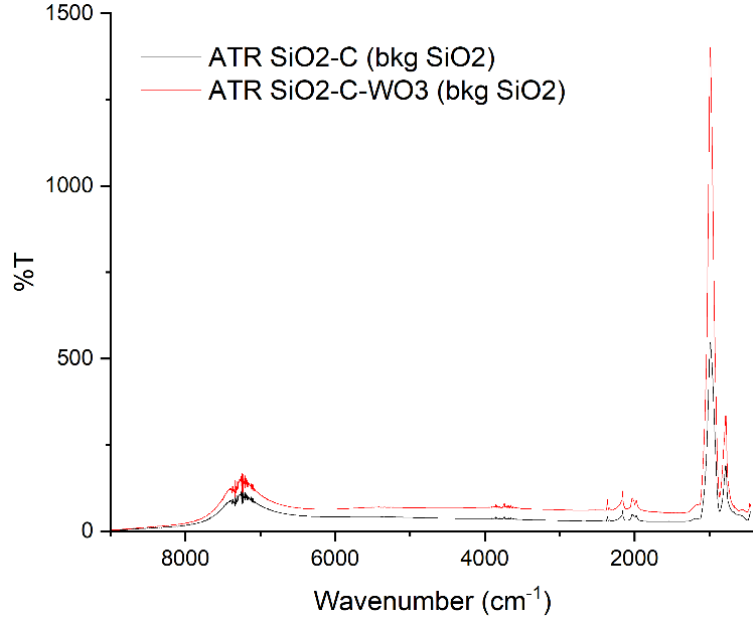


Figure 8: ATR spectrum of SiO₂–carbon. The dominant $\sim 900\text{ cm}^{-1}$ silica band reflects background issues. Absence of a $\sim 1700\text{ cm}^{-1}$ C=O band suggests limited oxidation of the carbon layer.

Specular reflectance. After adding WO₃, transmittance in the 5000–2000 cm⁻¹ window decreases markedly (Fig. 9). Two small features at $\sim 2198\text{ cm}^{-1}$ and $\sim 2360\text{ cm}^{-1}$ appear; assignment is uncertain (adsorbed CO₂ is a possibility). Below 2000 cm⁻¹ the spectrum was unreliable; we will prioritise ATR optimised for $< 1000\text{ cm}^{-1}$ to access WO₃ phonons.

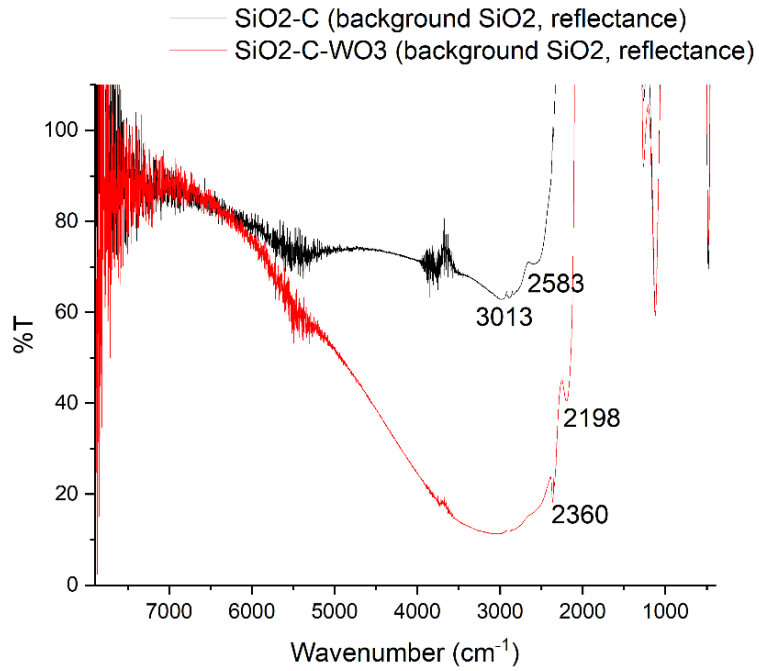


Figure 9: IR reflectance spectra before and after WO_3 deposition. Transmission decreases between $5000\text{-}2000\text{ cm}^{-1}$. Small peaks at 2198 and 2360 cm^{-1} appear after WO_3 , possibly due to adsorbed CO_2 .

Transmission. After carbon coating the IR transmission is nearly extinguished (Fig. 10); with the additional WO_3 layer the instrument could not acquire reliable data. Future IR work will thus focus on ATR with improved background.

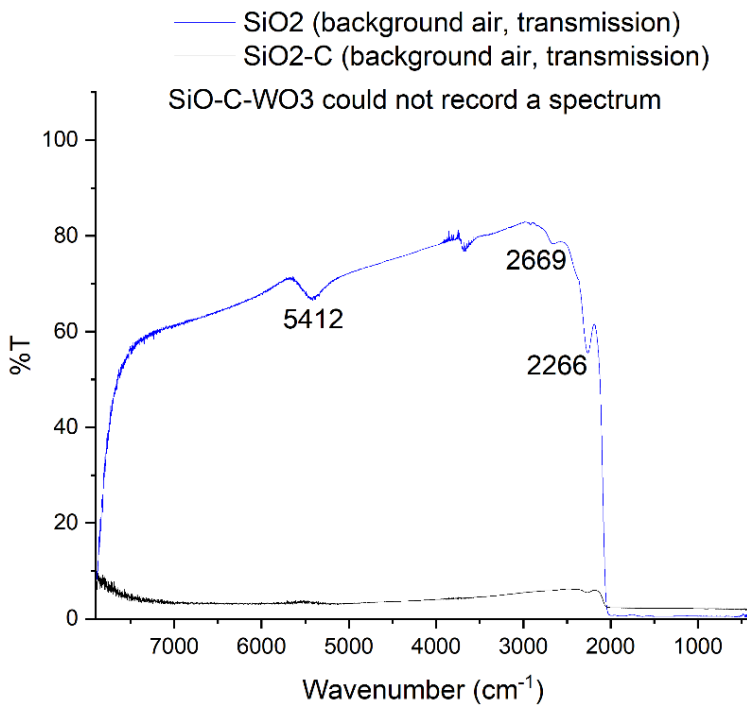


Figure 10: IR transmission spectra of SiO₂–carbon and SiO₂–carbon–WO₃. Transmission is strongly suppressed by the carbon layer; the WO₃-coated sample yields negligible signal.

6.4 Fluorescence (WO₃ sample)

The SiO₂–carbon–WO₃ sample shows a sharp excitation feature near 270 nm (Fig. 11); using 270 nm excitation yields an emission at \sim 370 nm and another at \sim 445 nm. Reported WO₃ emissions are broad and structure-dependent; the observed sharp peaks are unusual and may be real or instrument artefacts. We will re-run excitation–emission maps, include SiO₂ and SiO₂–carbon controls under identical conditions, and test additional excitation wavelengths to confirm reproducibility.

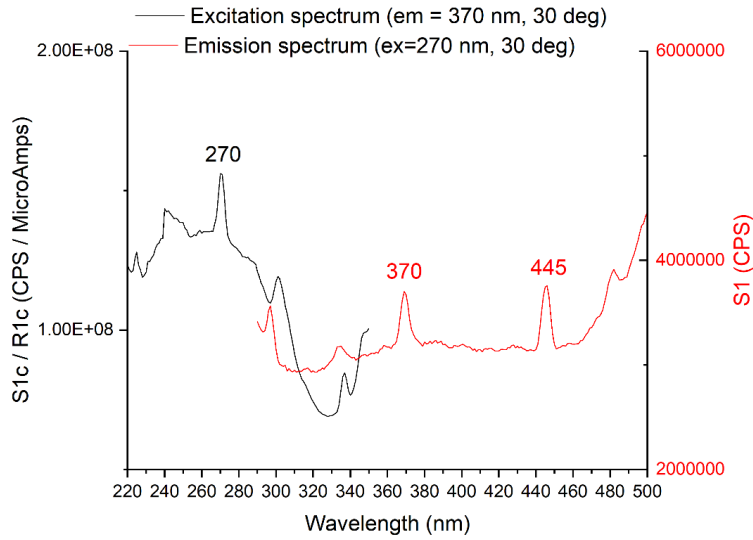


Figure 11: Excitation and emission spectra of the SiO_2 –carbon– WO_3 sample. A sharp excitation feature near 270 nm produces emissions at ~ 370 and ~ 445 nm, sharper than typical WO_3 luminescence.

6.5 UV–Vis absorbance

The carbon layer saturates absorbance ($A \approx 4$), transmitting roughly 0.01% of incident light; WO_3 features cannot be resolved in transmission. Reflectance-mode UV–Vis or ellipsometry will be more informative going forward.

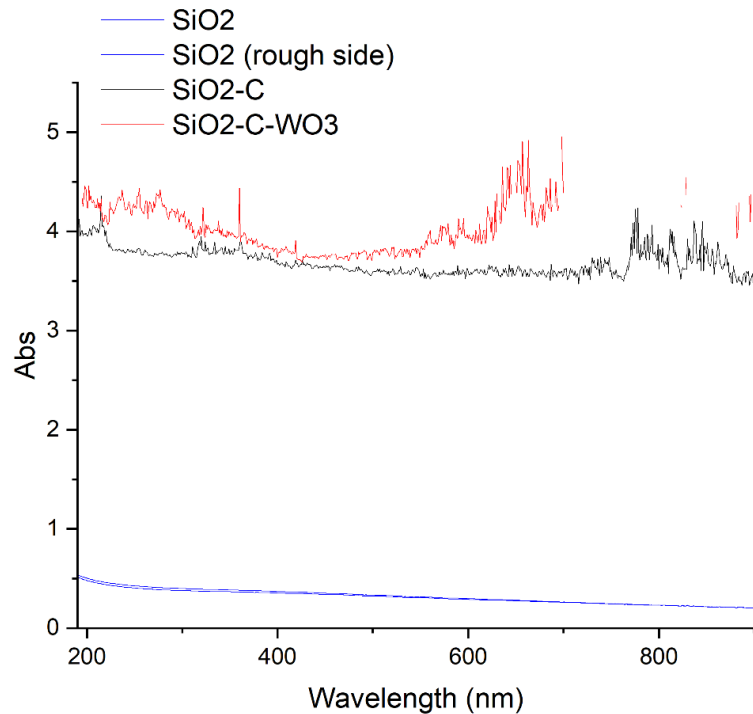


Figure 12: UV-Vis absorbance of the SiO_2 –carbon– WO_3 sample. The carbon layer yields near-total absorption ($A \approx 4$), preventing detection of WO_3 features in transmission mode.

Data and notes provenance

All numerical values, instrument conditions, and qualitative observations above reflect the teams September 2025 measurement notes and plots (Raman, IR, fluorescence, UV–Vis, XRD, XPS planning, and four-point probe planning). (Internal project document, Sept 2025).

Notes

- Deposition conditions were chosen on the basis of literature screening and prior in-house experiments for WO_3 on silica/FTO substrates.
- At present we have not confirmed whether the deposited carbon layer is graphene, reduced graphene oxide (rGO) or amorphous carbon - the chosen conditions follow reports that can produce graphene-like films, but definitive identification requires combined Raman, XPS and TEM analysis.

References

- [1] Georg Kresse and Jrgen Furthmller. Efficient iterative schemes for ab initio total-energy calculations using a plane-wave basis set. *Physical Review B*, 54(16):11169, 1996.
- [2] Georg Kresse and Jrgen Furthmller. Efficiency of ab-initio total energy calculations for metals and semiconductors using a plane-wave basis set. *Computational Materials Science*, 6(1):15–50, 1996.
- [3] Peter E Blchl. Projector augmented-wave method. *Physical Review B*, 50(24):17953, 1994.
- [4] Georg Kresse and Daniel Joubert. From ultrasoft pseudopotentials to the projector augmented-wave method. *Physical Review B*, 59(3):1758, 1999.
- [5] John P Perdew, Kieron Burke, and Matthias Ernzerhof. Generalized gradient approximation made simple. *Physical Review Letters*, 77(18):3865, 1996.
- [6] Stefan Grimme, Jens Antony, Stephan Ehrlich, and Helge Krieg. A consistent and accurate ab initio parametrization of density functional dispersion correction (dft-d) for the 94 elements h-pu. *Journal of Chemical Physics*, 132(15):154104, 2010.
- [7] Bjrk Hammer and Jens K Nrskov. Theory of adsorption and surface chemical bonding. *Advances in Catalysis*, 45:71–129, 2000.
- [8] Bjørk Hammer and Jens K. Nørskov. Why gold is the noblest of all the metals. *Surface Science*, 343(3):211–220, 1995.
- [9] Bjørk Hammer and Jens K. Nørskov. Theoretical surface science and catalysis calculations and concepts. *Advances in Catalysis*, 45:71–129, 2000.
- [10] X. Jiang, X. Nie, X. Guo, C. Song, and J. G. Chen. Recent advances in carbon dioxide hydrogenation to methanol via heterogeneous catalysis. *Chemical Reviews*, 120(15):7984–8034, 2020.
- [11] J. Zhong et al. State of the art and perspectives in heterogeneous catalysis of CO_2 hydrogenation to methanol. *Chemical Society Reviews*, 49:1385–1413, 2020.

- [12] S. Kattel, P. J. Ramírez, J. G. Chen, J. A. Rodríguez, and P. Liu. Active sites for CO_2 hydrogenation to methanol on Cu/ZnO catalysts. *Science*, 355(6331):1296–1299, 2017.
- [13] W. Zhang et al. Carbon dioxide conversion to methanol. *Frontiers in Energy Research*, 8:621119, 2021.
- [14] A. García-Trenco et al. CO_2 to methanol: routes, catalysts and techno-economics. *Nature Reviews Chemistry*, 5(8):564–579, 2021. Review covering heterogeneous, electro-, photo- and enzymatic routes; interfacial effects and TRL.